Analyst

ROYAL SOCIETY OF CHEMISTRY

PAPER

View Article Online
View Journal | View Issue

Cite this: *Analyst*, 2021, **146**, 4683

Cross-modality imaging of bisphosphonate-treated murine jawbones†

Susanne Reier,[a] Anna Turyanskaya,[b] Patrick Heimel,[c,d] Nikolaus Frischauf,[e] Daria Meusburger,[a] Thomas Heuser,[a] Nicole Drexler,[a] Ágnes Janovszky,[f] Christina Streli,[b] Paul Slezak,[c] Birgit Plochberger,[e] Peter Dungel,[c] Andrea Szabó[g] and Andreas Walter *[a]

In this proof-of-principle study, we established and implemented a cross-modality imaging (CMI) pipeline to characterize and compare bisphosphonate (BIS)-treated jawbones of Sprague-Dawley rats after tooth extraction after physical therapies (photobiomodulation and extracorporeal shockwave therapy (PBMT and ESWT)). We showcase the feasibility of such a CMI approach and its compatibility across imaging modalities to probe the same region of interest (ROI) of the same jawbone. Jawbones were imaged *in toto* in 3D using micro-Computed Tomography to identify ROIs for subsequent sequential 2D analysis using well-established technologies such as Atomic Force Microscopy and Scanning Electron Microscopy, and recent imaging approaches in biomedical settings, such as micro-X-Ray Fluorescence Spectroscopy. By combining these four modalities, multiscale information on the morphology, topography, mechanical stiffness (Young's modulus), and calcium, zinc and phosphorus concentrations of the bone was collected. Based on the CMI pipeline, we characterized and compared the jawbones of a previously published clinically relevant rat model of BIS-related osteonecrosis of the jawbone (BRONJ) before and after treatment with BISs, PBMT and ESWT. While we did not find that physical therapies altered the mechanical and elemental jawbone parameters with significance (probably due to the small sample size of only up to 5 samples per group), both ESWT and PBMT reduced pore thicknesses and bone-to-enamel distances significantly compared to the controls. Although focused on BIS-treated jawbones, the established CMI platform can be beneficial in the study of bone-related diseases in general (such as osteoarthritis or -porosis) to acquire complementary hallmarks and better characterize disease status and alleviation potentials.

Received 10th December 2020,
Accepted 14th May 2021

DOI: 10.1039/d0an02373f

rsc.li/analyst

Introduction

Bisphosphonates (BISs) are widely used for the treatment of rheumatologic and oncological diseases with bone metastasis and are commonly administered in osteolytic conditions.[1] BISs are pyrophosphate analogs in which oxygen is replaced by a carbon atom, resulting in a backbone P–C–P which is stable against enzymes with hydrolytic activity. Although BISs have a similar core structure, they also contain two side-chains or groups, R1 and R2, attached to the central carbon atom. All the recently developed BISs contain a hydroxy side-group at position R1, increasing their binding to bone. Differences in the physicochemical and biological properties of BISs are due to the differences in the R2 side-group, where the presence of nitrogen and its orientation within the R2 side-chain can influence their overall potency.[2,3]

BISs are generally classified as first (*e.g.*, etidronate and clodronate), second (*e.g.*, alendronate and pamidronate) or third generation (*e.g.*, zoledronate, ZOL (Fig. 1)). The main indications for ZOL are hypercalcemia of malignancy, multiple myeloma and bone metastases from solid tumors. The taxonomy of BISs based on their chemical structure, such as their nitrogen content, is clinically more relevant as more severe side-effects (*i.e.* BIS-related osteonecrosis of the jaw, BRONJ) have been attributed to BISs containing nitrogen.[1,4] The main

[a]*Austrian BioImaging/CMI, Vienna BioCenter Core Facilities GmbH (VBCF), Vienna, Austria. E-mail: andreas.walter@vbcf.ac.at*
[b]*Atominstitut, Austrian BioImaging/CMI, TU Wien, Vienna, Austria*
[c]*Ludwig Boltzmann Institute for Experimental and Clinical Traumatology in the AUVA Trauma Research Center, Austrian BioImaging/CMI, Vienna, Austria*
[d]*Core Facility Hard Tissue and Biomaterial Research, Karl Donath Laboratory, University Clinic of Dentistry, Medical University Vienna, Vienna, Austria*
[e]*University of Applied Sciences Upper Austria, Austrian BioImaging/CMI, Vienna, Austria*
[f]*Department of Oral and Maxillofacial Surgery, University of Szeged, Hungary*
[g]*Institute of Surgical Research, Faculty of Medicine, University of Szeged, Hungary*
†Electronic supplementary information (ESI) available. See DOI: 10.1039/d0an02373f

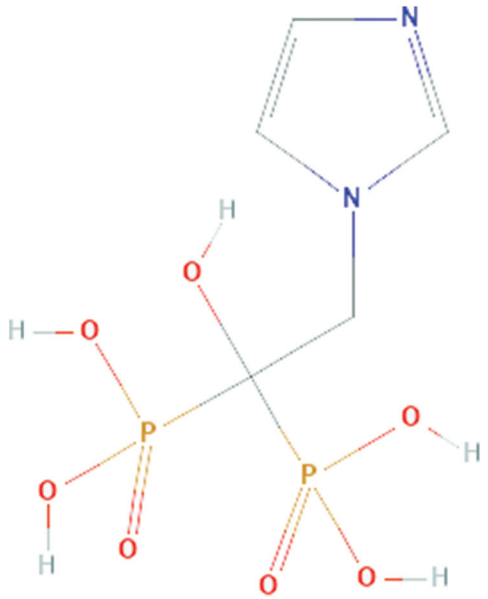

Fig. 1 Chemical structure depiction of zoledronate. From National Center for Biotechnology Information (2021). PubChem Compound Summary for CID 68740, zoledronic acid. Retrieved April 13, 2021 from https://pubchem.ncbi.nlm.nih.gov/compound/Zoledronic-acid.

therapeutic effect of BISs is linked to the inhibition of the activity and apoptosis induction of osteoclasts,[2,5] which leads to the inhibition of bone resorption and a reduction of bone turnover[5] and, hence, in an increase in mineral density.[6] Interestingly, the mechanism of action shows differences as a function of the nitrogen content. Non-nitrogen-containing BISs (etidronate and clodronate) are intracellularly incorporated, and their accumulation leads to osteoclast apoptosis by inhibiting ATP-dependent enzymes.[2,3] Inhibition of farnesyl diphosphate synthase is one of the modes of action of nitrogen containing BISs, leading to decreased functional activity and apoptosis of osteoclasts.[7]

Although BIS treatment undoubtedly improves the quality of life of the patients,[8] together with other antiresorptive[9] and antiangiogenic drugs,[10] BISs may induce necrosis of the oral bones (BRONJ). This occurs mainly after invasive dental procedures, *e.g.*, tooth extraction or a periodontal disorder,[1] with an increased incidence particularly after the use of third-generation BISs (*e.g.* ZOL).[5] The exact pathomechanism is not yet fully understood, but characteristics of drug administration (oral *vs.* intravenous (i.v.), non-/nitrogen-containing BIS, duration of the therapy), indication of BIS administration (osteoporosis, oncological reason), co-morbidities, concomitant use of other drugs (corticosteroids or chemotherapeutic drugs), poor oral hygiene or genetic factors may be considered.[11] Osteonecrosis develops typically several years after an invasive dental procedure, which may be explained by the long half-lives of these medications.[5] In our previous study,[12] BIS treatment was associated with mucosal healing disorders and some degree of discontinuity of the cortical and spongious bone regions in the mandible in a clinically relevant rat model of BRONJ.

Extracorporeal shock wave (ESWT) therapy has been well established in the field of orthopedics[13,14] for many years as a safe and non-invasive treatment option for indications like non-union fractures, chronic tendinopathies[15] or plantar fasciitis. Cell regeneration and pain release were main effects achieved through ESWT.[16,17] In recent years, the field of applications has become increasingly broader and now includes investigations into soft tissue[18] and nerve[19,20] regeneration as well as urology, trans-cranial and dental applications. In the dental field, for instance, ESWT applications have shown decreased tooth movement in rats in conjunction with increased osteoblast and osteoclast activities.[21] Furthermore, safety of dental ESWT was shown in human patients.[22,23] As such, the treatment modality was included in the experimental setup to study its effects on BIS-treated samples. Although ESWT is frequently used in medical treatments, the underlying effects are not yet known in detail.[24] ESWTs induce different chemical, mechanical and thermal effects in tissue. Thermal effects are created through interactions between compression and decompression and are proven to have no clinical relevance. The occurrence of free radicals is probable but also without relevance.[25] Cavitation through pressure change and occurrence of small gas-filled bubbles leads to jet streams (local high-speed liquid streams) in tissue. The effect of these streams is also not understood in detail but seems to be of high clinical relevance.[25,26] In brief, shockwave treatment consists of a series of mechanical pressure waves that are focused *via* an applicator that may be electrohydraulic, electromagnetic or piezo-electric.

Photobiomodulation therapy (PBMT) uses photons at non-thermal irradiance to promote biological activity. In general, PBMT makes use of light with a wavelength spectrum of 450–1200 nm (depending on the desired penetration depth) with low energy density (up to 1 W cm^{-2}). While lasers have been the gold standard as light sources, nowadays devices based on LED technology have come into the focus of research. PBM radiation initiates photochemical, photoelectric and photoenergetic reactions that affect the treated tissues by altering the metabolic functions of the cells and modulating biological processes. During the last few decades, numerous studies demonstrated the beneficial effects of light in the form of PBM for the treatment of various pathologies – although the exact cellular mechanisms responsible for the positive effects are not fully understood yet. Beside the promotion of wound healing and angiogenesis[27] and the reduction of inflammatory reactions,[28] the enhancement of bone formation represents an important field of application for PBMT. PBMT of bone tissue seems to improve the results of fracture repair, periodontal tissue, implant osseointegration and bone reconstruction with or without biomaterials (reviewed in ref. 29).

The appropriate management of BRONJ is still a challenge. Since conventional treatments are not always satisfactory, the use of adjuvant therapies is necessary. Recently, two case

reports showed the efficacy of PBMT, however in combination with antibiotics or platelet-rich plasma.[30,31]

A promising and novel approach to gain insights about the hallmarks of bone diseases holistically is cross-modality imaging (CMI). Currently, bioimaging is experiencing major boosts: the resolution revolution in electron cryo-microscopy (cryo-EM) led to an exponential increase in single particle structures and is accompanied by a 'volume revolution' that allows to scan big volumes at high resolution using for example focused ion beams and scanning electron microscopy (FIB/SEM). The same holds true for advanced light microscopy, which routinely resolves subcellular structures both below the diffraction limit (superresolution) and in thick tissue samples with increased penetration depth (light sheet and multiphoton microscopy). Spectroscopic imaging techniques are being used increasingly to characterize biomedical samples biophysically, assessing molecular (Mass Spectrometry Imaging, MSI), elemental (micro-X-Ray Fluorescence Spectroscopy, μXRF) or mechanical (Brillouin or Atomic Force Microscopy, AFM) information. In addition, the frontiers of bioimaging are currently being pushed towards the integration and correlation of these modalities to tackle biomedical research questions holistically and across multiple scales: CMI combines two or more complementary modalities that create a composite view of the sample and allow to access structural, functional and biophysical parameters from exactly the same sample from a single time point (Fig. 2). Novel CMI pipelines can bridge whole-animal imaging and *ex vivo* biological microscopy to zoom in from an intact sample to individual cells and combine localized biophysical or chemical information with structural and functional parameters.[32,59] Examples of correlative imaging pipelines that specifically unravel elemental 3D distributions include the work of De Samber *et al.*[57] and Gholap *et al.*[58] on the ecotoxicological model organism *Daphnia magna*: the results of μXRF were fused and co-registered into a morphological μCT 3D image,[57] and element-to-tissue correlation was obtained using μXRF and laser ablation-inductively coupled plasma-mass spectrometry.[58]

In this study, we showcase the feasibility of a novel CMI pipeline that comprises micro-Computed Tomography (μCT), μXRF, AFM and SEM (Fig. 4) to characterize the morphology, topography, mechanical stiffness and elemental concentrations of the jawbones of our clinically relevant rat model of BRONJ before and after treatment with BISs, PBMT and ESWT. We set up a workflow that was compatible across all imaging modalities and allowed the characterization of the same regions of interest (ROI) for each sample and technique (compare Fig. 4). The combination of the imaging modalities aimed at gaining morphological insights across length scales (from μCT at an isotropic voxel size of about 20 μm to SEM at sub-micrometer resolution) and complementing the morphological characterization by chemical (*i.e.*, the elemental concentrations of calcium (Ca), phosphorus (P) and zinc (Zn)) and mechanical imaging parameters (*i.e.*, the Young's modulus). Comprehensive imaging of BIS-treated jawbones ideally includes resolving the morphology at a (sub-)micrometer resolution to visualize for example microfractures at high resolution. Usually, for microscopy, penetration depth comes at the expense of lateral resolution, and visualizing a large volume of tissue at such high resolution is not possible (Fig. 2). Due to the established CMI pipeline, we were able to first visualize the entire intact jawbone in 3D at an isotropic resolution of 17.2 μm using μCT and then select a region of interest (ROI) that, after cutting of the bone, was scanned in 2D with increased lateral resolution of about 800 nm using SEM – in addition to adding elemental and mechanical infor-

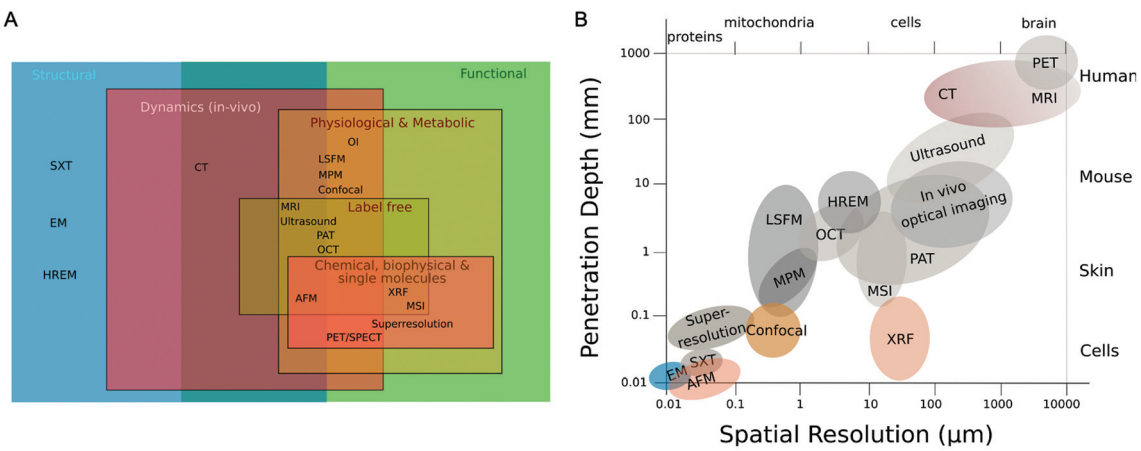

Fig. 2 Multiscale and holistic imaging: accessible information (A) and resolution (B) to CMI. Adapted from Walter *et al.*[32] SXT (soft X-ray tomography), HREM (high resolution episcopic microscopy), EM (electron microscopy), CT (computed tomography), OI (optical imaging including bioluminescence & fluorescence imaging), LSFM (light sheet fluorescence microscopy), MPM (multiphoton microscopy), confocal (microscopy), MRI (magnetic resonance imaging), ultrasound, PAI (photoacoustic imaging), OCT (optical coherence tomography), XRF (X-ray fluorescence spectroscopy), AFM (atomic force microscopy), MSI (mass spec imaging), superresolution (microscopy such as STORM, PALM, STED), PET/SPECT (positron emission tomography/single photon emission computed tomography).

mation using μXRF and AFM (see Fig. 4). So far, BIS-treated bones have been characterized largely using imaging modalities that reveal mainly structural parameters, and specific features of osteonecrosis have mainly been studied independently. This includes for example SEM to visualize osteocytic lacunae, Volkmann's or Haversian systems, immunofluorescence and histology to assess osteocyte necrosis, osteoclast numbers or osteocalcin, and computed tomography to measure bone sequestration and fragmentation.[32] There are only few studies that quantify and interrelate the effects of BISs on both the (micro)architecture and (biophysical) tissue properties of the jawbone. For example, BISs administered at high doses were shown to arrest the osteoblast cell cycle and to reduce the apatite crystal size, which may lead to altered mechanical characteristics.[32] Additionally, in rats, the onset of BRONJ was shown to correlate with increased unrepaired crack densities in the jawbone, which is likely to change its mechanical integrity.[33] While much of our understanding of BISs and their role in osteonecrosis originates from preclinical studies that involve a single imaging modality, it is desirable to characterize the effects of BISs and a corresponding onset of BRONJ in a broader context to develop therapeutic strategies. With the established CMI pipeline, we aimed at showcasing the feasibility of acquiring morphological, elemental and mechanical parameters from within the same ROI of the same jawbone using four complementary imaging modalities, and comparing them before and after BIS treatment and physical therapies (ESWT or PBMT) of the clinically relevant rat model of BRONJ.

Experimental

Study design

Twelve-week-old male Sprague-Dawley rats were treated with ZOL (80 μg kg^{-1} i.v. once a week, over 9 weeks) (n = 16) or with a saline vehicle instead of BIS (n = 3) (Fig. 3).[12] At the end of the third week of the protocol, the first and second molar teeth on the right side were extracted from the mandible in all of the BIS-treated animals under ketamine (25 mg kg^{-1} i.p.) and xylazine (75 mg kg^{-1} i.p.) anesthesia. The teeth were luxated with an 18G needle and the extraction was performed with extraction forceps. The roots were also removed with a dental drill under a Zeiss operating microscope (6× magnification, Carl Zeiss GmbH, Jena, Germany).

In one group of the BIS-treated animals (n = 6), rats were treated with local ESWT. An electrohydraulic applicator was used to focus the pressure wave from a high voltage spark to the target tissue after acoustic coupling. These focused pressure waves are characterized by a very fast initial pressure raise up to approximately 100 MPa within a few nanoseconds, followed by an elongated negative (tensile) pressure wave of lesser magnitude, providing a mechanic stimulus to the tissue. Immediately after the tooth extraction, shock wave treatment at 600 pulses at about 0.2 mJ mm^{-2} and 3 Hz were applied using the electrohydraulic Derma-Gold®100 device connected to a type OP155 applicator (Tissue Regeneration Technologies, LLC, manufactured by MTS Europe GmbH, Stuttgart, Germany). The applicator was placed directly on the skin above the location of the tooth extraction during the treatment.

In another BIS-treated group (n = 6), animals were locally treated by PBMT (with the diode placed directly on the lateral side of tooth extraction area) starting on the day of tooth extraction, which was followed by 7 more treatments every second day under light anesthesia with ketamine & xylazine (see above). Illumination was performed at room temperature for 90 s with a dose of 9 J cm^{-2} using a pulsed LED light of 635 nm (Repuls Lichtmedizintechnik GmbH, Vienna, Austria) at a pulse rate of 50% and a repetition frequency of 2.5 Hz. After each procedure the animals were kept in their original cages.

6 weeks after the invasive dental procedure, the animals were anesthetized with ketamine and xylazine (see above) and sacrificed. For all groups, the right mandible was removed, dissected free from the covering soft tissue, placed into a formaldehyde solution for 3 days for fixation, and embedded in paraffin for further μCT analysis. The *in vivo* part of the study was performed in accordance with the Guidelines of the National Institute of Health in the USA regarding the care and use of animals for experimental procedures and with the 2010/63/EU Directive and was approved by the Animal Welfare Committee of the University of Szeged, Hungary (V/1639/2013).

In a previous study, we had shown that tooth extraction in the presence of high dose of chronic ZOL treatment causes healing disorder in the jawbone in rats, which resembles the characteristics of BRONJ (ref. 12). These changes were demonstrated by comparing ZOL- and vehicle-treated groups (n = 10–10 animals) using micro-CT and histological analyses. As a continuation of this previous study, we tested the effect of physical therapies with an expanded set of parameters to not only visualize structural changes but also potential alterations in the composition of the bone in the affected region. In compliance with the 3R principle of animal experiments, we did not intend to repeat control groups (referred to as "negative and positive controls") in high animal numbers in the present study, but we used 6–6 animals in the ESWT- and PBMT-treated groups. The 'positive control' group included animals undergoing tooth extraction plus treatment with ZOL without any physical therapy, whereas 'negative controls' were subjected to an identical procedure except that these animals received saline as the vehicle of ZOL. Hence, these groups were indeed independent and were therefore subjected to statistical analysis accordingly.

μCT

Jawbones were scanned *in toto* in a SCANCO μCT 50 (SCANCO Medical AG, Brüttisellen, Switzerland) with 90 kVp, 200 μA with a 0.5 mm Al filter; 1000 projections per 180° with an integration time of 500 ms.

Fig. 3 Scheme of the study design. On the first week, chronic intravenous BIS treatment was initiated in 3 groups of animals, whereas the first group received a saline vehicle; this protocol was continued on every week. On week 3, the first and second molar teeth from the right mandibula were extracted (see X marked in red) in all of the groups. On the day of tooth extraction, a single event of a local ESWT treatment was performed in the third group, whereas in case of the fourth group, local PBM treatment was performed on the day of tooth extraction which was followed by additional 7 treatments every second day. Mandibles were harvested at the end of the protocol (6 weeks after the teeth were extracted) and processed according to the different imaging protocols. The first group is the negative control group since the animals only received saline solution intravenously. The second group is the positive control group and was treated with ZOL without any therapy.

Sample requirements and preparation. Samples were received embedded in paraffin with a soft tissue layer still present on the exterior of the bone, preventing the paraffin from infiltrating into the ROI.

Determination of the specimen position. For the 3D analysis of the µCT data, a volume of interest (VOI) was defined within the jawbone: it is the dense bone between the roots from the most apical piece of bone below the tooth to the tip of the first root or to where the bone transitions to a more porous morphology (about 1 mm^3). After the µCT scans and the identification of the VOI for each jawbone, the bone was then cut with a band saw (300CP, EXAKT Apparatebau, Norderstedt, Germany) through the center of the VOI, revealing a bone surface, which lies inside the µCT VOI. This cut through the µCT VOI defined the region of interest (ROI) that was analyzed in 2D by the subsequent imaging modalities. In plane, the ROI is limited by the 4 roots (the bone surface of the periodontal ligament space) and between the roots by a straight line at the narrowest point between adjacent roots (about 750 × 1000 µm). To ensure proper cutting, the cutting plane was positioned in a 3D rendering of the µCT reconstruction and then transferred to the physical sample. The band saw is equipped with a laser that indicates the cutting line. By comparing this cutting line with where the plane intersects the 3D model, it is possible to accurately position the cut. Two parallel cuts were performed with a distance of 3 mm, resulting in a 3 mm thick slice of the jawbone that was analyzed further using the subsequent modalities. A region of interest (ROI) was defined on the surface of this jawbone slice within the VOI and subsequently assessed in 2D by µXRF, AFM and SEM. The images shown in Fig. 5 were passed on to the subsequent modalities to facilitate the re-identification of the ROI on the cut samples.

Resolution. Scans were reconstructed to an isotropic resolution of 17.2 µm.

Data analysis. Measurements were performed within the VOI using the open-source image processing package ImageJ2/FIJI (https://imagej.net/Fiji).[34–36] Scans were rotated so that the dentin-enamel junction (DEJ) lied parallel to the XY plane and the teeth were aligned along the *Y* axis. The VOI was drawn between the roots of the first molar using the polygon tool and interpolation tools. Negative controls were measured at the third molar. The VOI was segmented with a threshold of 750 mgHA cm^{-3}, and the bone volume, tissue volume and pore sizes were measured using the BoneJ plugin (v.1.3.11).[38]

The distance of the alveolar bone crest to the DEJ (bone-to-enamel distance) was measured using Amira 5.4.7 (Thermo Fischer Scientific, Waltham, MA, USA). A dynamic slice was placed through the center of the mesial and distal roots and the center of the crown of the first molar. The bone-to-enamel distance was measured at three parallel positions: at the center of the distal root and in the middle between the center and the buccal and lingual edge of the distal root.

µXRF

µXRF imaging was performed using the laboratory setup at TU Wien, Atominstitut; the detailed description of the in-house-built µXRF spectrometer can be found elsewhere.[37] The instrument is equipped with a Rh-anode low power X-ray tube, and a Si(Li) detector (active area 30 mm^2, LN_2-cooled) with an ultrathin polymer window to allow the measurement of the low energy fluorescence radiation emitted by light elements. The primary beam was focused by a polycapillary optic (full lens) into a micro-beam with the size of 50 × 50 $µm^2$ at Cu-Kα (determined using a standard test sample). For all samples, the tube voltage and current were set to 50 kV and 0.4 mA, respectively. All measurements were performed in vacuum, and, for all scans of the ROI, the step size was 50 µm and measurement time 60 s per point.

Sample requirements and preparation. The cut jawbone was fixed onto an Al-frame metal plate and positioned vertically in the spectrometer chamber using a magnetic stage, so that the standard geometry of 45° between the incident radiation beam and the sample, and 90° between the incident beam and the detector is maintained.

Determination of the specimen position. Using a light microscope (Olympus Highlight 3100, Hamburg) integrated in the µXRF setup, the ROI was identified and corner points of the area to be scanned were determined. The ROI spanned about 750 × 1000 $µm^2$. Once the corner points had been set, the ROI was scanned with a step size of 50 µm and a dwell time of 60 s, lasting between 5 to 7 hours. In addition, the roots delineating the ROI were clearly distinguishable in the µXRF scans due to their low signals for all three elements (Ca, P, Zn) (compare Fig. 6A).

Resolution. The resolution of 50 µm (corresponding to the beam diameter and step size) was determined by scanning a Cu-wire with a thickness of 10 µm. The resolution was defined as $FWHM_{beam} \approx \sqrt{FWHM^2_{profile} - d^2_{wire}}$, where d is the wire diameter – see ref. 37 for further details. Using the mass

attenuation coefficients ($\mu\rho$) for cortical bone from the National Institute of Standards and Technology (https://physics.nist.gov/PhysRefData/XrayMassCoef/ComTab/bone.html) and a theoretical density (ρ) for hydroxyapatite of 3.16 g cm^{-3}, one can estimate the information depth for various elements in bone (*e.g.* Ca-K: 24 μm, Zn-K: 60 μm).

Data analysis. The fitting of the spectra was necessary to subtract the background and to ensure that the presented results corrected for sum or pile-up peaks. QXAS-AXIL[38] was used for deconvolution, and elemental maps of calcium, phosphorus and zinc were prepared with LP-map software (Fig. 6A). Using Fiji, based on their signal counts, elemental distributions were then measured and normalized to the scanned ROI excluding holes and microfractures as determined by SEM analysis. The μXRF concentrations were quantified using the sensitivity values obtained *via* the measurements of IAEA animal bone (H5) certified reference material; details can be found here.[39]

AFM

The Young's modulus was determined using nanoindentation with a JPK nanowizard 3 instrument (JPK BioAFM Business, Berlin, Germany). The used measurement mode (JPK's QI-mode) enabled topographical imaging and determination of the elastic properties simultaneously. Cantilevers with diamond-like carbon tip coating (PPP-NCHR, k = 42 N m^{-1}, f_0 = 336 kHz, NanoWorld, Switzerland) were used. The maximum indentation force was set to 20 μN. The z-length of sampling was determined as 2 μm and the piezo driving rate was set to 40 nm ms^{-1}.

Sample requirements and preparation. Before measuring, samples were cleaned with ethanol and distilled water to remove embedded paraffin residues (which would lead to strong interactions between the measuring tip and sample). Measurements were performed in phosphate buffered saline (PBS) at room temperature. Bone pieces were fixed to microscope glass slides (VWR, Austria) with a two-component adhesive (Z-Dupe – Shore-A20, Henry-Schein, Austria) for easy removal afterwards.

Another requirement for AFM indentation measurements is the nanoscopic flatness of the samples. Since the measuring tip can be located at a maximum distance of 15 μm from the sample surface (restriction/movement possibility of the piezo), the samples must have a roughness below ~10 μm – which was achieved by the clear bandsaw cut as described above.

Determination of the specimen position. Re-identification of the ROI was facilitated by a combined and fully synchronized single molecule sensitive fluorescence and atomic force microscope: a JPK nanowizard 3 instrument (JPK BioAFM Business, Berlin, Germany) was placed on top of the JPK Motorized precision stage (Brucker, Berlin) that is mounted on a Zeiss Observer Z1 epifluorescence microscope body. The combined microscope is placed on a passive anti-vibration table without additional active damping (Newport). For experiments, the cantilever was first aligned to the optical axis *via* the XY positioning unit on the motorized JPK precision stage. The two instruments were synchronized *via* TTL signals.

Measurements were carried out on at least three samples of each treatment group within the same ROI as defined for μXRF and SEM (compare Fig. 4). Depending on the surface roughness, one (256 × 256 pixels, 65 536 data points) or two measurements (128 × 128 pixels, 16 384 data points) were performed for each sample on an area of 90 × 90 μm^2 inside the ROI. Within each ROI, three to six 90 × 90 μm^2 areas were scanned.

Resolution. Force curves were recorded for each pixel in an area of 90 × 90 μm^2, resulting in a lateral spatial resolution of about 700 nm for acquisitions of 128 × 128 pixels and of about 350 nm for acquisitions of 256 × 256 pixels. The penetration depth results from the indentation depth which ranged from 2 nm up to 8 nm (compare Fig. 4). The force resolution depends on the system. In our system, the noise was smaller than 6 pN.

Data analysis. Fitting of the Oliver-Pharr model to the QI data and determination of the Young's modulus were achieved using the batch processing interface of the JPK SPM data processing software.[40,60] The model predicts the depth of indentation (according to the tip geometry) and gives the Young's modulus for each curve. For each pixel, a single force curve was collected, resulting in up to ~65 000 data points per 90 × 90 μm^2 area. The Young's modulus per sample is given as an average of these data points with three to six scanned 90 × 90 μm^2 areas per ROI. Fig. 4 shows a representative force distance (indentation) curve together with the fitted model and extracted value.

SEM

Samples were examined with a Hitachi TM-1000 tabletop scanning electron microscope operated at 15 kV and equipped with a high-sensitive semiconductor backscattered electron detector.

Sample requirements and preparation. The samples were rinsed with distilled water to remove potential phosphate residues from PBS (used in AFM measurements). Samples were sputtered with a 4 nm gold layer in a Balzers SCD 050.

Determination of the specimen position. Due to the clear visibility of the roots in the backscattered electron channel, the roots could be used as landmarks with a clear delineation of the ROI. The same ROI as for μXRF of about 750 × 1000 μm^2 was scanned.

Resolution. The pixel size for the highest magnification was 800 nm and corresponds to the lateral resolution.

Data analysis. Fiji was used to analyze the average microfracture size and microfracture density of the samples. Each microfracture within the same ROI as for the other modalities was marked by freehand selection, and its area was measured (Fig. 7A). The threshold to analyze the average microfracture size was set to above 10 μm^2 to exclude minimal lesions or cracks. Using Fiji, the percentage of microcracks within the ROI (*microfracture density*) and the average crack size in the

ROI were determined and compared across the 4 different groups.

Data analysis

Analysis of the acquired images was carried out as described in the Experimental section of each modality to obtain a parameter cloud per sample group.

For the comparison of the measured parameters across the different groups, we explored the data by employing the statistical computing software environment R v3.6.3.[41] The data were plotted in boxplots using the packages ggplot2 (https://CRAN.R-project.org/package=ggplot2) and ggpubr (https://CRAN.R-project.org/package=ggpubr). A one-way analysis of variance (ANOVA) was conducted to analyze differences in the mean values between the four groups (PBMT, ESWT, Neg-Ctrl and Pos-Ctrl). We checked for normality using the Shapiro–Wilk-test and tested for homogeneity of variances using the Levene-test (package "car", https://CRAN.R-project.org/package=car). Due to non-normality, a non-parametric Kruskal–Wallis-test with a further Dunn-test with Bonferroni correction (package "dunn.test", https://CRAN.R-project.org/package=paran) was conducted for Zinc, microfracture size, microfracture density and pore thickness. The significance level was set at 0.05.[42]

For the comparison of all acquired parameters per ROI independent of their group, a correlation matrix was produced using the package stats v3.6.3 and visualized using the package corrplot v0.84.[43] Due to unequal sample sizes in the four variables PBMT, ESWT, Neg-Ctrl and Pos-Ctrl we applied a pairwise deletion for missing data treatment. Since the missing values are not related to the other variables in the data set (missing completely at random) and the proportion of missing data did not exceed 20%, pairwise deletion can be considered as an appropriate technique.[44] The numerical correlation coefficients of the correlation matrix can be found in the ESI (Table S2†).

Results & discussion

The showcased CMI pipeline comprised four complementary modalities: μCT, μXRF, AFM and SEM. Each modality contributed a different length scale or biophysical parameter to the characterization of the jawbone. Mechanical information on the stiffness of the jawbone and chemical information on the elemental composition were contributed by AFM and μXRF and complemented the imaging modalities that typically assess morphology (μCT and SEM). The combined imaging modalities were chosen such that they complemented each other while still ensuring compatibility concerning the sample preparation workflow. SEM and AFM achieved the highest resolution but required sectioning of the bone, μCT achieved modest resolution in comparison to SEM but allowed to image the entire intact bone and provided overall context, and μXRF hardly gave structural context but added otherwise inaccessible information about the elemental composition.

The established CMI workflow is illustrated in Fig. 4: we distinguish between the VOI for μCT (about 1 mm^3) as the only imaging technology that assessed the jawbone in 3D and the ROI of about 750 × 1000 μm for all subsequent technologies that only assessed the 2D topography of a cut section within the VOI of the jawbone. The VOI for μCT is located below the first molar (see Fig. 5) and indicates the volume in which the bone parameters were measured (in 3D): two of the three molars were extracted in each sample. Around the extraction sites, the bone exhibited highly irregular changes with large differences between all samples and occasional tooth fragments still embedded in the bone. This made the choice of a robust VOI difficult. For this reason, the dense homogeneous bone between the roots of the intact molar was chosen as VOI (from the most apical piece of bone below the tooth to the tip of the first root or to where the bone transitions into a more porous morphology). Changes at this site were less severe than at the extraction site but, due to its proximity, this region had received doses of ESWT and PBMT similar to those of the extraction site itself. The sample was then cut with a band saw through the center of the VOI, revealing a bone surface (ROI), which lay inside the μCT VOI (compare Fig. 4 and Experimental). For all subsequent modalities, measurements were performed within this ROI, which was limited in 2D by the four roots and by a straight line at the narrowest point between adjacent roots. Re-identification of this ROI after relocation between the modalities was facilitated by (i) the integration of light microscopes into the μXRF and AFM platforms and by (ii) its delineation by the four roots that were clearly visible in μXRF and SEM (see Fig. 6 and 7). μXRF and SEM scanned the entire ROI for each sample, whereas AFM measurements were limited to at least three selected areas of 90 × 90 $μm^2$ within the ROI due its nanometer precision and long measuring time per pixel (Fig. 4).

To facilitate correlation of the data across modalities, we scanned the same ROI of about 1000 × 750 $μm^2$ of each sample sequentially and without compromising data quality. With correlation, we refer to identifying this ROI of a single sample after relocation between imaging platforms, including the quantification of (averaged) values from the ROI and their comparison both across differently treated groups and modalities. We did not co-register the data pixelwise. Since, based on the μCT reconstructions, the ROI was chosen such that it covered only homogeneous dense bone, it was sufficient to average the information obtained from the ROI (such as elemental concentrations and mechanical stiffness) and compare it across modalities. We nevertheless required precise imaging technologies to ensure that measurements were only taken from within the clearly delineated ROI. In addition, a pixelwise correlation would be hampered by the large differences in pixel size across modalities (for AFM and μXRF, for example, the pixel size was 350 nm and 50 μm, respectively).

On the macroscopic scale, we used *ex vivo* μCT to visualize the entire intact jawbone of several millimeters in thickness and the contextual morphology at an isotropic resolution of

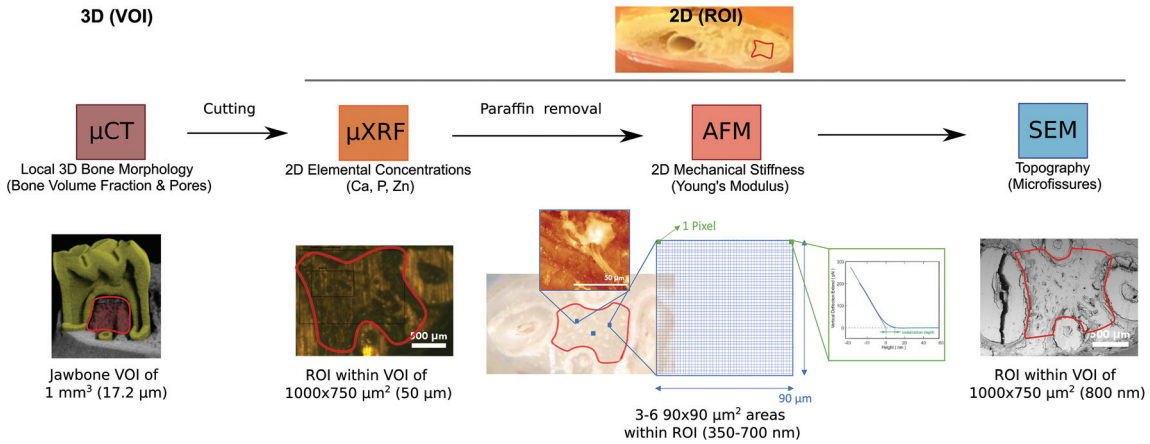

Fig. 4 Synopsis of the CMI workflow to visualize multiparametric jawbone features for the clinically relevant murine model of BRONJ before and after treatment with BISs, ESWT and PBMT. The modalities were applied sequentially. Textboxes below the modality name indicate the measured bone parameters for each technology (*i.e.*, morphology, elemental concentrations, mechanical stiffness, and topography). The color code is based on Fig. 2A. The images from the single modalities indicate in red the VOI for µCT and the ROI for µXRF/SEM and AFM. The texts below the images specify the scanned VOI and ROI and show the achieved resolution in parentheses: the entire jawbone was scanned in 3D at 17.2 µm resolution using µCT, and a VOI of about 1 mm^3 was defined based on the µCT reconstruction to analyze the bone morphology, including the bone volume fraction and pore thicknesses. The jawbone was cut through the center of the VOI, and the cut surface was further analyzed in 2D using µXRF, AFM and SEM. Based on the VOI, the ROI for µXRF and SEM was defined (indicated in red) and is delineated by the four roots of the first molar tooth. For µXRF, the elemental concentrations for each sample were averaged across this ROI. For AFM, from within the ROI, at least three areas of 90 × 90 μm^2 (blue squares in the brightfield image) were selected and scanned to acquire topography and Young's moduli (up to 65.000 data points). One data point was recorded within each pixel (green square), and all data points across the 90 × 90 μm^2 areas within one ROI were then averaged to yield the Young's modulus for the sample. The right image under AFM shows a representative indention curve, acquired within one pixel. The *x*-axis reflects the nanoscopic movement of the measuring tip in the direction towards the sample surface. Once the probe tip has deformed the surface, the probe tip experiences linear bending with force. The region between the first contact and the linear bending specifies the indentation depth that corresponds to the penetration depth.

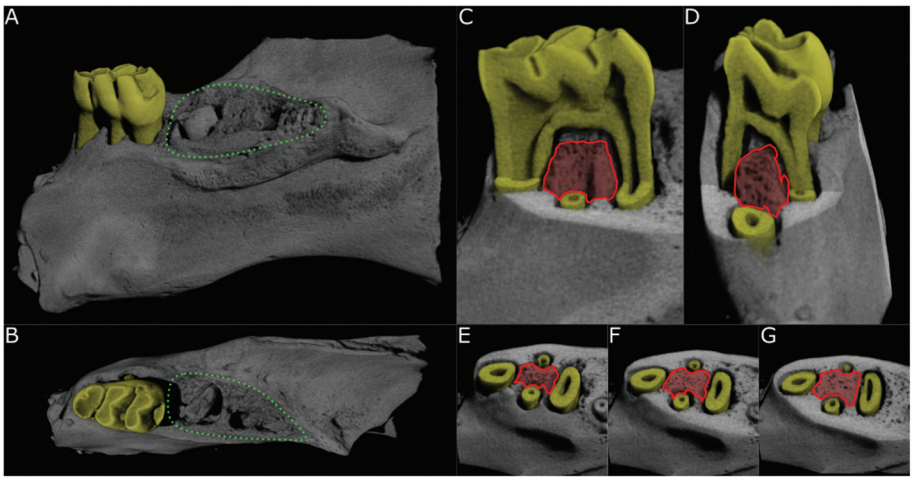

Fig. 5 Selection of the 3D VOI based on the µCT scan of a negative control sample. (A) View of the extracted piece of jaw from the lingual side. Tooth extraction site circled in green; first molar highlighted in yellow. (B) View from coronal side. (C, D) Cut-through center of the first molar from lingual (C) and mesial (D) sides; VOI highlighted in red. (E–G) Horizontal cuts through the VOI at the top, center and bottom layer of the VOI.

17.2 µm. µCT provided quantitative 3D information about the local dense bone morphology within the VOI as described in the Experimental section (Fig. 5). The non-destructive measurements of µCT made it possible to choose an appropriate plane within the VOI (ROI) for further 2D investigation using µXRF, AFM and SEM.

Within the µCT VOI, the bone volume fraction (bone-to-tissue volume (BV/TV)) and pore sizes were measured. The bone volume fraction describes the volume of mineralized bone per unit volume of the sample; the threshold was set to 750 mg cm^{-3} hydroxyapatite. The bone volume fraction is expected to decrease and the pore size to increase in necrotic

bones. The distance between the alveolar crest and the DEJ (bone-to-enamel distance) was measured on the intact molar on the side adjacent to the extraction for at least four data points per sample. The distance is assumed to increase in cases of disturbed homeostasis and misbalances of the bone tissue as a result of alveolar bone loss.[45]

For cross-modality imaging, the information from the μCT scans was then used to cut each sample through the center of the VOI at exactly the same position and angle as explained in the Experimental section. As the VOI was only around 1 mm^3 in volume, sectioning had to be accomplished at high precision using a diamond-coated band saw since the other modalities depended on a highly reproducible cut and a low roughness of below 10 μm to enable the combination of the modalities on a single sample. Without the information from the μCT to plan the sectioning, this would not have been possible with the required precision. After cutting, the pictures in Fig. 5 were created and passed along to subsequent modalities to ease identification of the ROI for subsequent modalities.

The macroscopic information for each VOI was then complemented by measurements of the elemental composition within the 2D ROI at a pixel size of about 50 μm using μXRF (Fig. 6A). Elemental maps were obtained by raster-scanning the jawbone ROI surface. The spatial resolution depended on the size of the X-ray beam. In this setup, the beam was focused to a size of 50 μm, therefore, the lateral resolution is in the same range (compare Experimental). The final elemental concentrations per sample were averaged across the ROI. The depth resolution (penetration depth) is element dependent. Further information on the method can be found in ref. 46.

μXRF allowed the semi-quantitative assessment of the sample: within each spectrum (obtained from a single scan point), the area under the peak of the element of interest was estimated by the software and translated into counts. The calcium, phosphorus and zinc levels were assessed by measuring the mean signal intensity in the ROI of their corresponding elemental maps and translated into concentrations using standard reference material (see Experimental). Examples of calcium, phosphorus and zinc maps are shown in Fig. 6A. This is the same sample as shown in Fig. 5 (μCT), 6B (AFM) and 7 (SEM) and indicates the same ROI (dashed red line) across modalities. Phosphorus and calcium are the two major constituents of hydroxyapatite ($Ca_{10}(PO_4)_6(OH)_2$), the primary bone component. Due to their occurrence in hydroxyapatite, both elemental maps of calcium and phosphorus are expected to show the same trends. Zinc and strontium are the trace elements that are normally found in bone tissue.[47] Zinc acts in many ways on the formation and remodelling of bone tissue. On the molecular basis, it stimulates alkaline phosphatase (ALP) activity, resulting in an increased mineralization process.[48] For necrotic bones, a decrease in calcium and phosphorus levels is expected since a lower bone mineral density is thought to be directly related to lower hydroxyapatite levels. However, osteonecrosis is a localized phenomenon which may occur only at some portions of the tooth extraction site in response to BIS. Conversely, BIS *per se* increases the mineral density in the bone (at the tooth extraction site and also in most of the bones of the body), since BISs suppress osteoclasts and slow the remodelling process while they can still induce BRONJ as a severe side effect.[6]

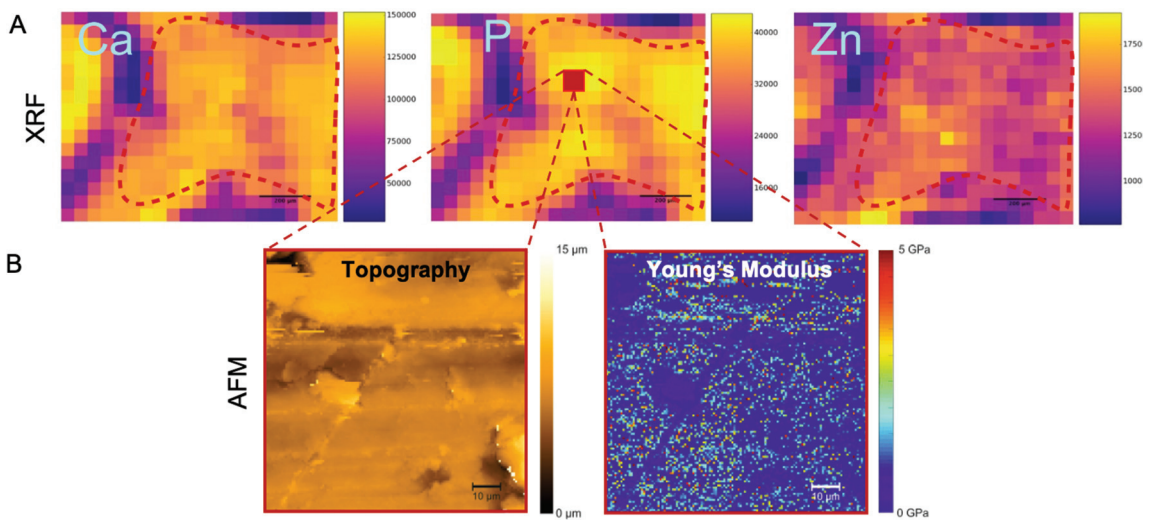

Fig. 6 AFM and μXRF of the same sample as shown in Fig. 5 and 4 for a truly correlative approach. (A) μXRF elemental distributions showing calcium (left), phosphorus (middle) and zinc (right) maps (in counts). The ROI is delineated by the red dashed lines. The legend to the right of each image shows the pixel intensity. Purple areas (low pixel intensity) mainly correspond to the non-mineralized tissue around the teeth roots. Scale bars: 200 μm. (B) AFM nanoindentation measurements show the sample topography (left) and the distribution of Young's moduli (right) in a fraction from within the ROI as explained above (a selected area of 90 × 90 $μm^2$). This area is indicated in the phosphorus map (red square). This 90 × 90 $μm^2$ area was scanned by AFM (as indicated by the dashed red lines) to simultaneously measure topography and Young's modulus, using JPK QI mode. Representative data are shown for the same negative control sample of Fig. 5 and 7. Young's moduli (in GPa) were calculated using the Oliver Pharr model.

μXRF was shown to be an ideal modality for correlative imaging and this CMI pipeline in particular. Re-identification of the ROI was achieved using the attached light microscope at the μXRF setup (compare Experimental). Due to its clear delineation by the four roots, the ROI could be unambiguously detected. The advantage of μXRF over other elemental imaging techniques (*e.g.* secondary ion mass spectrometry, laser ablation inductively coupled mass spectrometry) is its non-destructiveness, which facilitates the combination with other imaging modalities.[49–51] In addition, μXRF provided the necessary spatial resolution to precisely delineate the ROI and only measure within this region. μXRF has rather straightforward requirements in terms of sample preparation: flat smooth surfaces, and, in the case of non-confocal μXRF (as applied in the current project), thin samples are preferred to minimize the influence of element-dependent information depth. In most cases, preliminary embedding is performed since embedding preserves the tissues, aids in cutting/polishing, and a portion of the embedding medium around the tissue helps to maintain the shape of a thin section and facilitates its mounting on the sample stage. The paraffin embedding of the jawbones was, therefore, well-fitting to the requirements of μXRF. For the subsequent modalities after μCT (see Fig. 4), paraffin-embedded jawbone sections were warmed up to +60 °C in an embedding station to remove paraffin.

All structural and elemental data were complemented by mechanical parameters that assessed the stiffness within the ROI (Young's modulus) using AFM, as described in Experimental. While the sample was scanned at submicrometer resolution, a single Young's Modulus was given for each sample and used for comparison since it was averaged across the scanned areas of about $90 \times 90\ \mu m^2$ from within the ROI of homogeneous dense bone tissue (see Fig. 4 and 6). To determine the stiffness and elastic properties of the jawbones, we measured the Young's modulus using AFM-nanoindentation (see Experimental). AFM nanoindentation uses a cantilever with a characterized tip geometry as indenter, which allowed for a high spatial resolution in the nanometer range. For the determination of the Young's modulus, the measured force data were fitted with the Oliver Pharr model (see Experimental).

The values for the Young's moduli varied from a few tenths of GPa to up to 5 GPa for a single area of $90 \times 90\ \mu m^2$ within the ROI, depending on the location of the measurement (Fig. 6B, right). Although the ROI was chosen to be as homogeneous as possible, this might also be due to the different layers of bone tissue which provide different mechanical strengths. While the cortical bone, for example, needs to withstand daily compression and is therefore stiff, the trabecular bone (also called spongy bone) hosts blood vessels and bone nerves and has a lower Young's modulus. For the rat mandibulae, a Young's modulus of about 3 GPa had been measured previously.[52] For necrotic bones and increased porosity, we expected a decreased mechanical stiffness; for higher bone mineral density, we expected higher Young's moduli.[53]

For cross-modality imaging using AFM, paraffin was removed after μXRF imaging, and the cut jawbones were additionally washed with Ethanol to remove potential paraffin remains and minimize background noise. This was followed by moistening the samples with PBS. With the AFM-attached light microscope (see Experimental), the ROI was identified based on its delineation by the tooth roots. Importantly, similar to the other combined modalities, AFM does not need staining or labeling of features of interest, which facilitated cross-modality imaging.

On the microscopic scale, the topography of the cut jawbone was visualized using SEM at a resolution of about 800 nm. This resolution allowed to identify and measure microfractures in the ROI. Microfractures are a typical pathophysiological indication of BRONJ due to bone loss and destruction. Assuming that BIS-treated animals will exhibit more microfractures, we used SEM to determine the density and area of microfractures (Fig. 7). We quantified two parameters: (i) microfractures density within the ROI, and (ii) the average microfracture size. In contrast to the pore thicknesses assessed by μCT, the average microfracture size is measured in 2D at higher resolution. μCT pores were, in principle, only detectable in 2D if spanning at least two pixels (*i.e.*, at least 300 μm^2 for a pixel size of 17.2 μm), whereas microfractures were unambiguously identified and discerned above a size of about 10 μm^2 (which we set as the minimal threshold after data analysis).

For cross-modality compatibility, as shown in Fig. 4, SEM was applied as the last imaging modality of the established CMI pipeline since it required a thin gold coating to counteract electrical charging – the coating would have hindered AFM measurements.

Novel CMI pipelines (including more than two modalities) are still in their infancy since they require considerable method development due to the lack of commercially available implementations. CMI faces several challenges: (1) preparation steps for one imaging technique are often incompatible with those of another, (2) workflows and markers are missing that facilitate tracking and correlation of ROIs after relocation between imaging platforms, (3) many advanced imaging techniques might simply not be available or accessible to a single researcher,[61] and (4) CMI requires a broad expertise to oversee several modalities.[32] Our CMI pipeline required substantial coordination and careful sample preparation procedures that were compatible across all modalities without compromising data quality (including the sequence of experiments). Main points to take into consideration included a flat cut of the jawbone after μCT for all the subsequent imaging modalities (AFM specifically required a sample roughness of below ~10 μm), removal of paraffin after μXRF for the AFM measurements, and a thin gold coating before SEM. The precise selection of the VOI and ROI was enabled by μCT and flat band saw cuts. For μXRF and AFM, the subsequent re-identification of the 2D ROI on cut sections was possible due to their integrated light microscopes in hybrid setups. In addition, the identification of the ROI was facilitated across modalities due

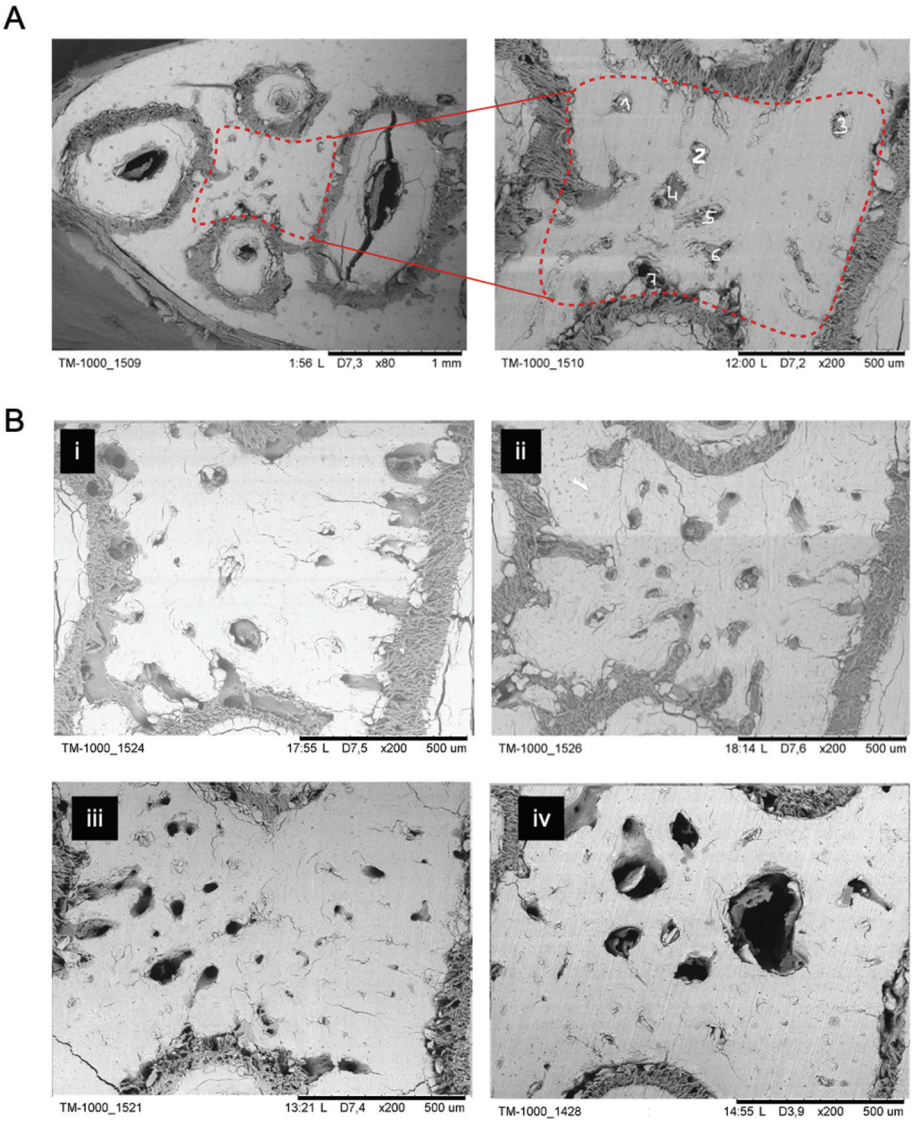

Fig. 7 (A) Overview SEM image at ×80 magnification of exactly the same sample and ROI as selected by μCT. The rectangle marks the ROI. To the right the ROI is shown at 200× magnification – including the counted microfractures. (B) SEM images of the ROI at a magnification of ×200. (i) Non-treated jawbone of the negative control group, (ii) BIS-treated animals of the positive control group, (iii) ESWT animals, and (iv) PBMT animals.

to its delineation by the roots that produced a clearly discernible signal across different contrast mechanisms in SEM, μXRF and light microscopy as integrated in the AFM setup (Fig. 5–7).

In addition, the established CMI pipeline provided us with a versatile tool to (a) characterize BIS-treated jawbones in comparison to untreated tissue, (b) assess the effects of physical PBMT and ESWT in terms of morphology, elemental composition and stiffness after BIS treatment, and (c) establish interdependencies between all measured parameters across modalities:

(a) Although differences between the untreated negative control group and BIS-treated groups were observed across all modalities (compare Table 1 and Fig. 8), the differences were not shown to be significant, which could be due to the small sample size of only up to 5 samples per group. In our study, the data nevertheless indicated clear trends of the averaged parameter values across groups and provided useful additions to the observed mucosal healing disorders and discontinuity of the cortical and spongious bone regions in the mandible of treated *versus* untreated groups, observed in our previous study on this clinically relevant rat model of BRONJ.[12]

In terms of morphological parameters, we observed a decrease in the average pore thickness, microfracture size and bone-to-enamel distance in all BIS-treated groups compared to the negative control, while, at the same time, the average microfracture density increased for all BIS-treated groups. There was a trend towards a higher bone fraction volume after BIS treatments. BIS-treated samples, independent of the physical therapies they received, seem to be more prone to the

Table 1 Synopsis of averaged measured parameters with standard deviations

	CT			µXRF			AFM	SEM	
	Pore thickness [µm]	Bone-to-enamel distance [µm]	BV/TV [%]	Ca [mg g^{-1}]	P [mg g^{-1}]	Zn [µg g^{-1}]	Young's modulus [GPa]	Microfracture density [%]	Ø microfracture size [µm^2]
Neg Ctrl	67 ± 5	1.65×10^3	84 ± 3	$(2.1 \pm 0.3) \times 10^2$	$(1.5 \pm 13) \times 10^2$	$(7.2 \pm 0.2) \times 10^2$	1.5 ± 0.1	1.5 ± 1.3	$(3.2 \pm 2.3) \times 10^3$
Pos Ctrl	61 ± 6	$(1.2 \pm 0.2) \times 10^3$	85 ± 3	$(2.4 \pm 0.3) \times 10^2$	$(1.6 \pm 9) \times 10^2$	$(9.4 \pm 0.2) \times 10^2$	1.2 ± 0.1	2.3 ± 1.2	$(1.7 \pm 0.5) \times 10^3$
ESWT	58 ± 3	$(0.6 \pm 0.2) \times 10^3$	86 ± 3	$(2.4 \pm 0.2) \times 10^2$	$(1.5 \pm 0.1) \times 10^2$	$(9.7 \pm 0.6) \times 10^2$	1.1 ± 0.6	2.5 ± 0.6	$(1.6 \pm 0.6) \times 10^3$
PBMT	56 ± 3	$(0.8 \pm 0.2) \times 10^3$	87 ± 4	$(2.4 \pm 0.2) \times 10^2$	$(1.5 \pm 0.1) \times 10^2$	$(9.5 \pm 0.5) \times 10^2$	1.1 ± 0.4	2.1 ± 0.6	$(2.6 \pm 0.9) \times 10^3$

accumulation of small-sized microfractures, which, in turn, reduces the average values for the measured pore and microfracture sizes. It was found previously in animal studies that BIS could increase the microdamage frequency in a dose-dependent manner, caused by excessively suppressed bone turnover.[33] The accumulation of microfractures might contribute to the deterioration of the biomechanical bone integrity and contribute to the onset of BRONJ. Contrary to expectations, the negative control group exhibited a large bone-to-enamel distance. However, samples with residual root fragments directly adjacent to the measurement site were excluded, leaving only a single sample for the negative control group, which is why further analysis and correlation of more samples will be needed to draw definite conclusions.

In our study, the accumulation of microfractures was accompanied by a decrease in the mechanical stiffness of the jawbones. On average, BIS-treated samples exhibited lower Young's moduli compared to the untreated control group. The stiffness of bone was found previously to be highly dependent on its porosity, and Young's moduli decrease nonlinearly with increasing pore densities.[53]

While the increase in microfracture densities after BIS treatment hints towards reduced mechanical and physiological bone integrity that might be prone to BRONJ, in terms of elemental composition, on average, all measured concentrations of calcium, phosphorus, and zinc increased after BIS treatment and indicated increased bone stability. Increased calcium and phosphorus concentrations are in line with the expectations for BIS treatment since BISs, *per se*, increase bone mineral density ubiquitously as they accelerate osteoclast apoptosis and inhibit bone resorption.[6,54] Zinc deficiency was shown to be associated with bone growth retardation, and an increase in zinc concentrations might be beneficial for the development, growth, and health of the bone.[55,56]

(b) Our results did not indicate that the applied PBMT or ESWT influenced bone alterations considerably concerning the mechanical and elemental composition since the measured parameters of these groups did not change significantly compared to the BIS-treated positive controls that did not receive physical therapies (Fig. 7). However, ESWT and PBMT exhibited a trend towards smaller pore thicknesses compared to the negative control (Kruskal–Wallis chi-squared = 10.329, d_f = 3, p-value = 0.016), which might be due to the overall increase in microfracture densities after BIS treatment. The differences in pore thickness were significant between PBMT and the negative control (*Post-hoc* Dunn, p = 0.007). In terms of bone-to-enamel distance, both the ESWT and PBMT group revealed notably smaller averaged values as compared to the positive and negative control groups (ANOVA, F = 10.86, d_f = 3, p = 0.003) – a hint for improved homeostasis and alveolar bone turnover after the physical therapies. The differences were significant between ESWT and the positive (*Post-hoc* Tukey, p = 0.021) and negative control (*Post-hoc* Tukey, p = 0.006), as well as between PBMT and the negative control (*Post-hoc* Tukey, p = 0.013). Since zinc plays a critical role in numerous physiological processes, including bone homeostasis,

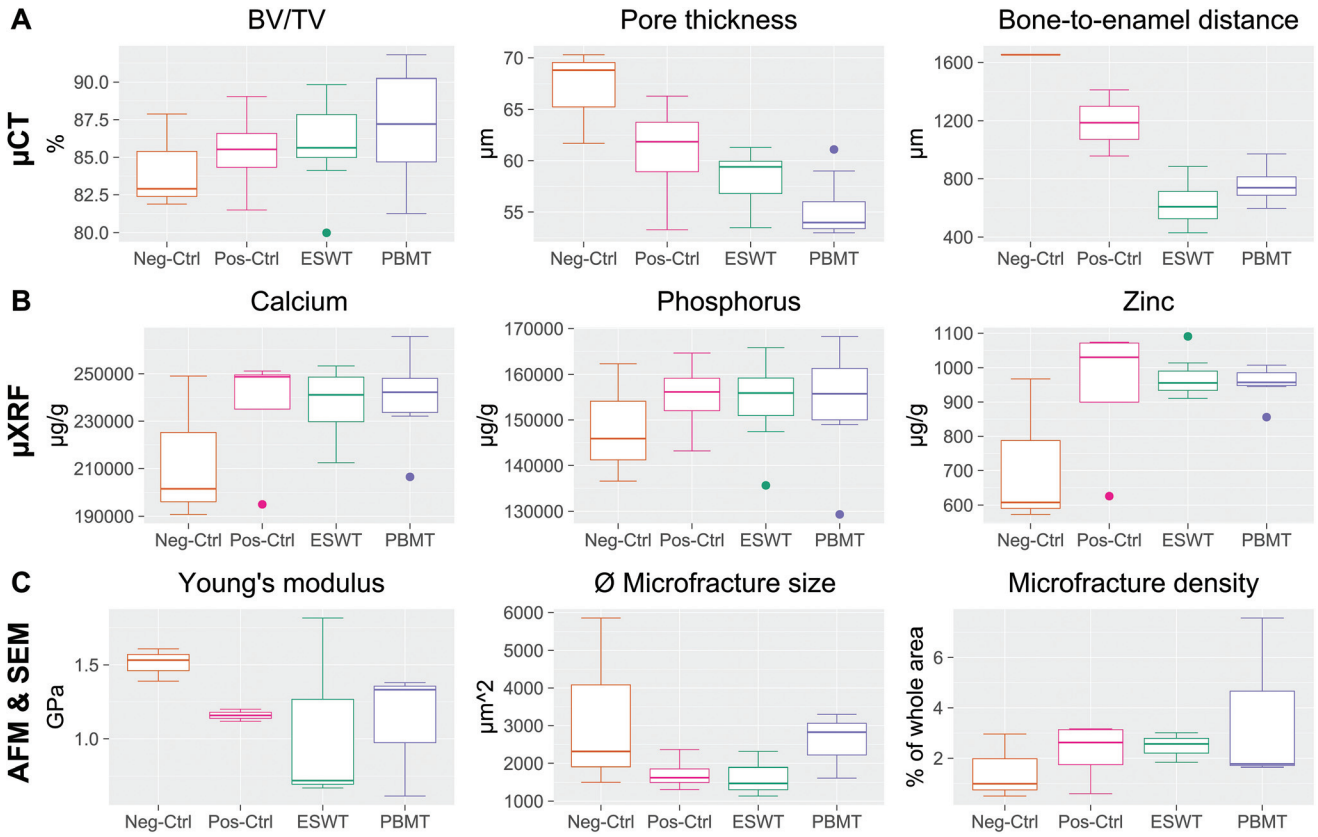

Fig. 8 Measured parameter sets per modality to characterize jawbones across the different groups. (A) Pore thickness, bone-to-enamel distance and bone volume fraction (BV/TV) as quantified by µCT. No significant difference was observed between BIS-treated samples and negative controls, but a consistent tendency of the BIS-treated bones for higher BV/TV average values, and smaller average pore thickness. The ESWT values of bone-to-enamel-distances differed significantly in comparison to the negative (p = 0.006) and positive control (0.021), as well as the PBMT values in comparison to the negative control (0.013). For the pore thickness, the difference between the PBMT group and the negative control was shown to be significant (p = 0.007). (B) Calcium, phosphorus and zinc concentrations as assessed by µXRF. As expected, calcium and phosphorus concentrations show the same trends due to their occurrence in hydroxyapatite. On average, all BIS-treated jawbones show increased calcium, phosphorus and zinc concentrations as compared to the negative control group. (C) Young's modulus measured by AFM. The graph shows the mechanical stiffness of bone samples. On average, the stiffness decreased for BIS-treated jawbones. (D) Average microfracture size and microfracture density as assessed by SEM. Despite no significant differences, a tendency can be observed: all BIS-treated animals exhibit a higher average microfracture density with on average smaller microfracture sizes as compared to the negative control group (compare also Table 1). For all boxplots, the median is given as a line in the box. The boxes themselves comprise the interquartile range (lower to upper quartile); the whiskers show the minimum and the maximum. Outliers are indicated as points.

microstructural stability and bone remodeling, these findings are also in line with the tendency of increased zinc concentrations after both ESWT and PBMT (Table 1).

(c) The novel pipeline allowed to establish interdependencies between the different morphological, topographical, elemental and mechanical parameters that had been analyzed by the 4 modalities. These correlations were assessed independent of the group: since each ROI was measured by each modality and probed for each of the parameters shown in Fig. 8 and Table 1, the showcased CMI pipeline allowed to establish correlations from within the same area of a single specimen. Correlations are shown in the correlation matrix of Fig. 9, and the corresponding correlation coefficients are given in Table S2.† We observed both cross-modality and inner-modality interdependencies. As can be appreciated in Fig. 9, in our study, the Young's modulus as measured by AFM correlated positively with the average microfracture size and pore thickness, but negatively with the elemental concentrations as measured by µXRF and with the microfracture density as probed by SEM: the smaller the average microfracture size and pore thickness, the lower the Young's modulus; the higher the microfracture density and the elemental concentrations, the lower the stiffness of the bone. This is in line with our findings in (a) – and reveals two unexpected trends: (1) a positive correlation between pore size and mechanical stiffness; (2) a weak negative correlation between mineral density and mechanical stiffness (compare Fig. 9). As pointed out in (a), the first correlation can be explained by the assumption that a decrease in the average pore and microfracture size is due to the increase in the amount of small-sized microfractures after BIS treatment and a corresponding higher microfracture density, *i.e.* a lower mechanical stiffness correlates with smaller pore sizes

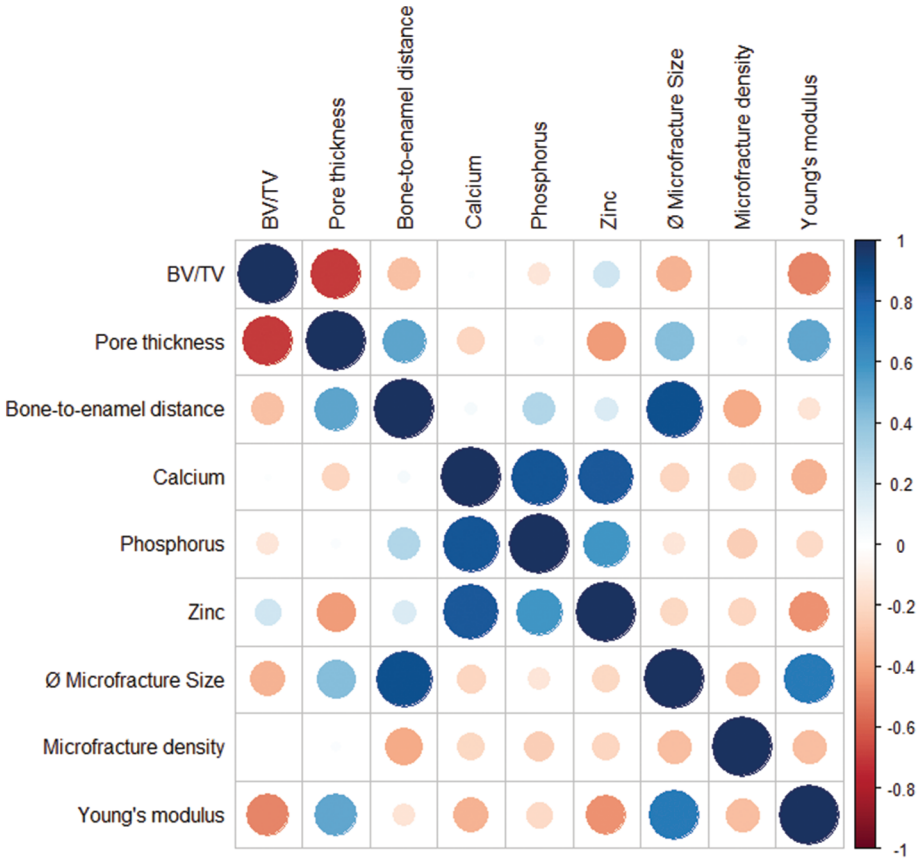

Fig. 9 Correlation matrix of morphological, mechanical and elemental properties. Interdependencies of parameters from within the same ROI independent of their group can be established both across modalities and within a modality dataset. Blue circles indicate a positive, red circles a negative correlation. Circle size and color scheme correspond to the correlation coefficient (dark color and big circles correspond to highly correlated, light color and small circles to uncorrelated data). See also ESI, Table S2.†

due to a higher microfracture density. A possible explanation for the second correlation for the decrease in mechanical stiffness despite the BIS-induced increase in mineral densities (Ca/P/Zn) can be the destabilizing effects of the simultaneous microfracture accumulations.[53] In addition, the average microfracture size as measured by SEM correlated positively with the bone-to-enamel distance as assessed by μCT.

Within the parameter clouds assessed by a single modality, positive correlation was revealed among elemental concentrations of zinc, calcium and phosphorus. This is only logical since phosphorus and calcium are the two major constituents of hydroxyapatite ($Ca_{10}(PO_4)_6(OH)_2$), the primary bone component, and zinc can occur in the mineral component, probably in hydroxyapatite or in complex with fluoride, which might improve the crystallinity of apatite.[56] Negative correlation was revealed among the CT parameters and is also little surprising: the bigger the measured pore thickness, the smaller will be the bone volume fraction. Interestingly, we did not find significant correlations between elemental distributions and the morphology of the bone (microfractures, porosity or bone volume fraction) – except for a weak negative correlation between zinc concentrations and pore thicknesses.

Conclusion

The aim of this project was to showcase the feasibility and compatibility of a CMI pipeline across modalities for measuring and comparing diverse jawbone parameters (morphology, mechanical stiffness, elemental concentrations) before and after treatments with BIS and physical therapies. With the established imaging pipeline, current limitations of the single modalities (*i.e.* the restriction of each technique to only one resolution and information space) were overcome due to the complementary combination of the modalities. Each technique contributed unique parameters to the characterization of treated and untreated jawbones according to its strengths. While *ex vivo* μCT represented a good tradeoff between high resolution and broad field of view (the entire 3D morphology of the jawbone), it did not provide physical or chemical parameters. Biophysical characteristics (the stiffness of the jawbone as quantified by the Young's modulus) were provided by AFM in 2D and complemented by the 2D assessment of the elemental composition (calcium, phosphorus, and zinc concentrations) of each jawbone by μXRF. SEM zoomed in onto the surface of the cut jawbone and characterized the topography (microfractures) at (sub)micrometer resolution. The pipe-

line provides a versatile tool to interrelate biophysical properties and structure of exactly the same bone and will foster the integration between multiscale and multimodality data sets in preclinical bone models. Although CMI promises great potential in holistically characterizing BIS-treated bones and diseases in general, it presents several challenges from a technical point of view that need to be overcome. The routine use of CMI in biomedical research, including this specific pipeline, will need to aim at automation to create statistical throughput – specifically since the presented pipeline is time-consuming and needs careful logistics and modified sample preparation protocols due to the variety of involved modalities. Specifically, markers, workflows and software are missing that facilitate tracking and correlating ROIs after relocation between imaging platforms and allow automated registration and correlation of different images and parameters of diverse modalities. While we restricted our analysis to averaged values from within a well-defined ROI of about 0.75 mm^2, pixelwise co-registrations across modalities (as achieved for example in[57]) can yield element-to-tissue correlations at micrometer accuracy.

In addition to the development of the CMI pipeline, our approach provided insights into the characteristics of BIS-treated jawbones and assessed the changes induced by physical therapies. Using CMI, we integrated a variety of structural and biophysical information of a single jawbone. Across the 4 different groups, we revealed changes after BIS treatments in the morphology (pore thickness, bone-to-enamel distance, microfracture density and average size), stiffness (Young's modulus) and elemental composition (calcium, phosphorus and zinc concentrations) of the jawbone, but the pipeline did not highlight PBMT or ESWT as physical therapies that had a significant effect on the measured bone parameters or re-established untreated characteristics (although ESWT and PBMT reduced pore thicknesses and bone-to-enamel distances significantly). Interestingly, the average values for both microfracture densities and calcium, phosphorus and zinc concentrations increased consistently after BIS treatment. Across all samples independent of their treatment and group, the established CMI pipeline revealed a variety of interdependencies between the measured parameters of the modalities. For example, as pointed out in the results section, in our case, a decrease in stiffness was accompanied by an increase in the microfracture density and, surprisingly, an increase in calcium, phosphorus and zinc concentrations. Further correlation studies are needed to confirm our findings with statistical significance and to rule out any effect of the fixation with formaldehyde on mineral content of the bone. For future studies, this CMI pipeline can be used as a versatile tool for researchers to assess bone diseases holistically and help to identify biomarkers in osteonecrosis. CMI will surely be a routine approach in future biomedical research and diagnostics, once its achievements are showcased in further CMI pipelines, and higher throughput will be facilitated by automation and easy access to high-end imaging infrastructure and expertise.

Author contributions

SR conducted the correlation analysis, including box plots, ANOVA and the correlation matrix, and helped to draft the article. AT contributed to the acquisition of the microXRF data and analyzed them. PH acquired the microCT data and analyzed them. NF contributed to the acquisition of the AFM data and analyzed them. DM contributed to the acquisition of the microXRF and SEM data and helped to analyze them. ND and TH contributed to the acquisition of the SEM data. CS supervised the microXRF analysis.

PS participated in the *in vivo* experiments, planned and performed the applications of the biophysical treatments, and supervised the microCT analysis. BP supervised the AFM analysis. PD participated in the *in vivo* experiments, planned, performed and supervised the applications of the biophysical treatments, and contributed to the manuscript. AJ carried out the *in vivo* experiments. AS designed, planned, carried out and supervised the *in vivo* experiments, and contributed to the manuscript. AW designed, planned, and supervised the pipeline and all cross-modality analyses and correlations, and drafted the article.

Conflicts of interest

There are no conflicts to declare.

Acknowledgements

This work was supported by GINOP-2.3.2-15-2016-00034 granted to AS. This article was facilitated by the COST Action COMULIS (CA17121), supported by COST (European Cooperation in Science and Technology). The Electron Microscopy Facility of the Vienna BioCenter Core Facilities GmbH acknowledges funding from the Austrian Federal Ministry of Education, Science & Research and the City of Vienna.

References

1 S. L. Ruggiero, T. B. Dodson, J. Fantasia, R. Goodday, T. Aghaloo, B. Mehrotra and F. O'Ryan, *J. Oral Maxillofac. Surg.*, 2014, **72**, 1938–1956.
2 G. A. Rodan, *Annu. Rev. Pharmacol. Toxicol.*, 1998, **38**, 375–388.
3 M. J. Rogers, J. C. Crockett, F. P. Coxon and J. Mönkkönen, *Bone*, 2011, **49**, 34–41.
4 R. E. Marx, *J. Oral Maxillofac. Surg.*, 2003, **61**, 1115–1117.
5 M. A. Brozoski, A. A. Traina, M. C. Z. Deboni, M. M. Marques and M. da G. Naclério-Homem, *Rev. Bras. Reumatol.*, 2012, **52**, 265–270.
6 I. Coskun Benlidayi and R. Guzel, *ISRN Rheumatol.*, 2013, **2013**, 1–6.

7 S. P. Luckman, D. E. Hughes, F. P. Coxon, R. G. G. Russell and M. J. Rogers, *J. Bone Miner. Res.*, 1998, **13**, 581–589.
8 K. Kerschan-Schindl, J. Patsch, S. Kudlacek, A. Gleiss and P. Pietschmann, *Wien. Klin. Wochenschr.*, 2012, **124**, 532–537.
9 K. Niibe, T. Ouchi, R. Iwasaki, T. Nakagawa and N. Horie, *J. Prosthodont. Res.*, 2015, **59**, 3–5.
10 E. Serra, M. Paolantonio, G. Spoto, F. Mastrangelo, S. Tetè and M. Dolci, *Int. J. Immunopathol. Pharmacol.*, 2009, **22**, 1121–1123.
11 J. Yamashita, L. K. McCauley and C. Van Poznak, *Curr. Opin. Support. Palliat. Care*, 2010, **4**, 200–206.
12 Á. Janovszky, A. Szabó, R. Varga, D. Garab, M. Boros, C. Mester, N. Beretka, T. Zombori, H.-P. Wiesmann, R. Bernhardt, I. Ocsovszki, P. Balázs and J. Piffkó, *Clin. Oral Investig.*, 2015, **19**, 1279–1288.
13 J. Rompe, F. Rumler, C. Hopf, B. Nafe and J. Heine, *Clin. Orthop. Relat. Res.*, 1995, **321**, 196–201.
14 W. Schaden, A. Fischer and A. Sailler, *Clin. Orthop. Relat. Res.*, 2001, 90–94.
15 H. Lohrer, J. Schöll and S. Arentz, *Sportverletz. Sportschaden*, 2002, **16**, 108–114.
16 D. M. Wilbert, *BJU Int.*, 2002, **90**, 507–511.
17 C.-J. Wang, *Chang Gung Med. J.*, 2003, **26**, 220–232.
18 A. M. Weihs, C. Fuchs, A. H. Teuschl, J. Hartinger, P. Slezak, R. Mittermayr, H. Redl, W. G. Junger, H. H. Sitte and D. Rünzler, *J. Biol. Chem.*, 2014, **289**, 27090–27104.
19 T. Hausner, K. Pajer, G. Halat, R. Hopf, R. Schmidhammer, H. Redl and A. Nógrádi, *Exp. Neurol.*, 2012, **236**, 363–370.
20 D. Lobenwein, C. Tepeköylü, R. Kozaryn, E. J. Pechriggl, M. Bitsche, M. Graber, H. Fritsch, S. Semsroth, N. Stefanova, P. Paulus, M. Czerny, M. Grimm and J. Holfeld, *J. Am. Heart Assoc.*, 2015, **4**, e002440.
21 H. Hazan-Molina, I. Aizenbud, H. Kaufman, S. Teich and D. Aizenbud, in *Advances in Clinical Science*, ed. M. Pokorski, Springer International Publishing, Cham, 2016, pp. 57–65.
22 F. Falkensammer, C. Arnhart, C. Krall, W. Schaden, J. Freudenthaler and H.-P. Bantleon, *Clin. Oral Investig.*, 2014, **18**, 2187–2192.
23 E. B. Göl, N. Özkan, C. Bereket and M. E. Önger, *J. Craniofac. Surg.*, 2020, **7**, 2043–2048.
24 A. Notarnicola and B. Moretti, *Muscles Ligaments Tendons J.*, 2012, **2**, 33–37.
25 L. Gerdesmeyer, M. Maier, M. Haake and C. Schmitz, *Orthopade*, 2002, **31**, 610–617.
26 S. K. Shrivastava and Kailash, *J. Biosci.*, 2005, **30**, 269–275.
27 P. Dungel, J. Hartinger, S. Chaudary, P. Slezak, A. Hofmann, T. Hausner, M. Strassl, E. Wintner, H. Redl and R. Mittermayr, *Lasers Surg. Med.*, 2014, **46**, 773–780.
28 K.-T. D. Lee, M.-H. Chiang, P.-H. Chen, M.-L. Ho, H.-Z. Lee, H.-E. Lee and Y.-H. Wang, *Lasers Med. Sci.*, 2019, **34**, 913–920.
29 M. P. de O. Rosso, D. V. Buchaim, K. T. Pomini, B. B. D. Coletta, C. H. B. Reis, J. P. G. Pilon, G. Duarte Júnior and R. L. Buchaim, *Materials*, 2019, **12**, 4051.
30 C. Fornaini, L. Cella, A. Oppici, A. Parlatore, F. Clini, M. Fontana, G. Lagori and E. Merigo, *Laser Ther.*, 2017, **26**, 223–227.
31 M. Del Pilar Rodríguez-Sánchez, C. Statkievicz, J. M. de Mello-Neto, L. F. Toro, A. P. F. Bassi, V. G. Garcia, L. H. Theodoro and E. Ervolino, *J. Lasers Med. Sci.*, 2020, **11**, 98–103.
32 A. Walter, P. Paul-Gilloteaux, B. Plochberger, L. Sefc, P. Verkade, J. G. Mannheim, P. Slezak, A. Unterhuber, M. Marchetti-Deschmann, M. Ogris, K. Bühler, D. Fixler, S. H. Geyer, W. J. Weninger, M. Glösmann, S. Handschuh and T. Wanek, *Front. Phys.*, 2020, **8**, 1–47.
33 J.-W. Kim, M. E. A. Landayan, J.-Y. Lee, J. C. I. Tatad, S.-J. Kim, M.-R. Kim and I.-H. Cha, *Clin. Oral Investig.*, 2016, **20**, 2251–2258.
34 J. Schindelin, I. Arganda-Carreras, E. Frise, V. Kaynig, M. Longair, T. Pietzsch, S. Preibisch, C. Rueden, S. Saalfeld, B. Schmid, J.-Y. Tinevez, D. J. White, V. Hartenstein, K. Eliceiri, P. Tomancak and A. Cardona, *Nat. Methods*, 2012, **9**, 676–682.
35 C. A. Schneider, W. S. Rasband and K. W. Eliceiri, *Nat. Methods*, 2012, **9**, 671–675.
36 M. Doube, M. M. Kłosowski, I. Arganda-Carreras, F. P. Cordelières, R. P. Dougherty, J. S. Jackson, B. Schmid, J. R. Hutchinson and S. J. Shefelbine, *Bone*, 2010, **47**, 1076–1079.
37 S. Smolek, C. Streli, N. Zoeger and P. Wobrauschek, *Rev. Sci. Instrum.*, 2010, **81**, 053707.
38 IAEA, *Quantitative X Ray Analysis System*, International Atomic Energy Agency, Vienna, 2009.
39 V. Pichler, PhD Thesis, Technische Universität Wien, 2019.
40 W. C. Oliver and G. M. Pharr, *J. Mater. Res.*, 1992, **7**, 1564–1583.
41 R Core Team, *R: A Language and Environment for Statistical Computing*, R Foundation for Statistical Computing, Vienna, Austria, 2020.
42 J. C. F. de Winter, *Pract. Assess., Res. Eval*, 2013, **18**, 1–12.
43 T. Wei and V. Simko, *R package "corrplot": Visualization of a Correlation Matrix*, 2017.
44 M. M. El-Masri and S. M. Fox-Wasylyshyn, *Can. J. Nurs. Rese. Arch.*, 2005, **37**, 156–171.
45 T. L. Aghaloo, B. Kang, E. C. Sung, M. Shoff, M. Ronconi, J. E. Gotcher, O. Bezouglaia, S. M. Dry and S. Tetradis, *J. Bone Miner. Res.*, 2011, **26**, 1871–1882.
46 *Handbook of X-ray spectrometry: methods and techniques*, ed. R. van Grieken and A. Markowicz, Marcel Dekker, New York, NY, 1993.
47 B. Pemmer, A. Roschger, A. Wastl, J. G. Hofstaetter, P. Wobrauschek, R. Simon, H. W. Thaler, P. Roschger, K. Klaushofer and C. Streli, *Bone*, 2013, **57**, 184–193.
48 H.-J. Seo, Y.-E. Cho, T. Kim, H.-I. Shin and I.-S. Kwun, *Nutr. Res. Pract.*, 2010, **4**, 356.
49 D. S. Gholap, A. Izmer, B. De Samber, J. T. van Elteren, V. S. Šelih, R. Evens, K. De Schamphelaere, C. Janssen, L. Balcaen, I. Lindemann, L. Vincze and F. Vanhaecke, *Anal. Chim. Acta*, 2010, **664**, 19–26.

50 M. Rauwolf, A. Turyanskaya, A. Roschger, J. Prost, R. Simon, O. Scharf, M. Radtke, T. Schoonjans, A. Guilherme Buzanich, K. Klaushofer, P. Wobrauschek, J. G. Hofstaetter, P. Roschger and C. Streli, *J. Synchrotron Radiat.*, 2017, **24**, 307–311.
51 A. Svirkova, A. Turyanskaya, L. Perneczky, C. Streli and M. Marchetti-Deschmann, *Analyst*, 2018, **143**, 2587–2595.
52 G. Odin, C. Savoldelli, P.-O. Bouchard and Y. Tillier, *Med. Eng. Phys.*, 2010, **32**, 630–637.
53 M. B. Schaffler and D. B. Burr, *J. Biomech.*, 1988, **21**, 13–16.
54 J. Tamaoka, K. Takaoka, H. Hattori, M. Ueta, H. Maeda, M. Yamamura, K. Yamanegi, K. Noguchi and H. Kishimoto, *Exp. Ther. Med.*, 2018, **17**, 1440–1448.
55 M. Yamaguchi, *Mol. Cell. Biochem.*, 2010, **338**, 241–254.
56 T. Huang, G. Yan and M. Guan, *Int. J. Mol. Sci.*, 2020, **21**, 1236.
57 B. De Samber, G. Silversmit, K. De Schamphelaere, R. Evens, T. Schoonjans, B. Vekemans, C. Janssen, B. Masschaele, L. V. Hoorebeke, I. Szalóki, F. Vanhaecke, K. Rickers, G. Falkenberg and L. Vincze, *J. Anal. At. Spectrom.*, 2010, **25**(4), 544.
58 D. S. Gholap, A. Izmer, B. De Samber, J. T. van Elteren, V. S. Šelih, R. Evens, K. De Schamphelaere, C. Janssen, L. Balcaen, I. Lindemann, L. Vincze and F. Vanhaecke, *Anal. Chim. Acta*, 2010, **664**(1), 19–26.
59 K. Keuenhof, P. Heimel, L. M. Zopf, M. Raigel, A. Turyanskaya, A. Kavirayani, S. Reier, M. Glösmann, C. Schöfer, R. Kralovics, C. Streli, W. J. Weninger, S. H. Geyer, P. Slezak, K. Macfelda, R. Jäger, T. Wanek and A. Walter, Multimodality imaging beyond CLEM: Showcases of combined in-vivo preclinical imaging and ex-vivo microscopy to detect murine mural vascular lesions, *Methods in Cell Biology*, Elsevier, 2021, pp. 389–415.
60 W. C. Oliver and G. M. Pharr, *J. Mater. Res.*, 1992, **7**(6), 1564–1583.
61 A. Walter, G. J. Kleywegt and P. Verkade, Correlative multimodal imaging: Building a community, *Methods in Cell Biology*, Elsevier, 2021, pp. 417–430.